RSC Advances

ROYAL SOCIETY OF CHEMISTRY

www.rsc.org/advances

Journal Name

RSCPublishing

ARTICLE

Structural Evolution of OBC/Carbon Nanotube Bundle Nanocomposites under Uniaxial Deformation

Cite this: DOI: 10.1039/x0xx00000x

Siduo Wu,[a] Guangsu Huang,[a] Jinrong Wu [a] and Hui Li[a]

Received 00th January 2012,
Accepted 00th January 2012

DOI: 10.1039/x0xx00000x

www.rsc.org/

A regulated morphology of Multi-walled Carbon Nanotube Bundles (CNTBs) in Olefin Block Copolymer (OBC) matrix is achieved via solution blending after a short-time strong sonication which break CNTBs into smaller bundles. Inside the CNTBs which consist of several to dozens of nanotubes, the nanotubes exhibit a well aligned structure. A hybrid shish-kebab (HSK) superstructure is observed that the nanotubes in CNTBs act like central stem and OBC crystals periodically locate perpendicular to the axis of nanotubes. With 2 wt% incorporation of CNTBs, dramatic mechanical reinforcement is achieved with both tripled tensile strength and Young's modulus. The reinforcement might be resulting from efficient load-transfer brought by HSK superstructure as well as the unique bundle morphology of CNTBs with high robustness. In-situ small-angle X-ray scattering (SAXS) and wide-angle X-ray diffraction (WAXD) techniques were carried out to investigate the structural evolution of OBC and nanocomposites upon uniaxial deformation. With a considerable proportion of OBC crystals attached onto the surface of CNTBs, the scattered lamellaes in nanocomposites are of lower density. With the contribution from the larger long period of HSK superstructure and increased space between adjacent lamellaes, the long period of nanocomposites is remarkably increased. Upon stretching, the decrease of long period of neat matrix is dominated by the density of lamellaes, which increases upon the fragmentation of lamellaes. Inversely, the increase in the long period of nanocomposites is dominated by the stretching process, which leads to the increased separation of crystal lamellaes that are of lower density. The HSK superstructure in nanocomposites act as much larger but fewer hybrid crystal junctions, thus the OBC chains in nanocomposites are involved in even fewer physical junctions, indicating a less effective network structure than that of neat matrix. Thus the Hermans' orientation factor of both orthorhombic crystal and amorphous phases of nanocomposites are lower than that of neat matrix. With high incorporation of CNTBs and the prominent stereo hindrance brought by rigid CNTB network, the orientation behavior of nanocomposites doesn't comply to the slip-link theory.

1. Introduction

As one ideal couple for high-performance nanocomposites, one-dimensional nanofiller and crystalline polymers can exhibit various kinds of interfacial crystalline morphology [1-5]. For carbon nanotubes (CNTs) incorporated polymer crystallization, the most fascinating polymer crystalline morphology, the "hybrid shish-kebab (HSK)" superstructure can be achieved, wherein CNTs form central shish and disc-shaped polymer crystals periodically locate perpendicular to the tube axis [6]. Though the hybrid crystalline geometry is determined by the high surface curvature of nanotube surface considering the "size-dependent soft epitaxy (SSE)" mechanism, the kebab size could be easily controlled by regulating the crystallization environment [2]. With incorporation of CNTs, the HSK structure has been observed in various polymer matrix such as polyethylene (PE) [1,2,7], polyamide 6,6 (PA6,6) [1,2,8], polyvinylidene fluoride (PVDF) [9], polyvinyl alcohol (PVA) and poly(L-lactide) acid (PLLA) [10,11]. Nevertheless, no research on interfacial crystallization in low-crystallinity polymers has been reported, the main obstacle of which could be the statistical crystallizable block length and fringed micellar crystal morphology in conventional low-crystallinity polymers. Thus, if the polymer matrix contains highly ordered hard blocks that are long enough to chain fold, constructing interfacial crystallization could be practical. We take olefin block copolymer (OBC) as one consideration. Synthesized by a chain shuttling technology with highly ordered hard blocks and long rubbery soft segments, OBC can exhibit a lamellar crystal morphology even at the crystallinity of 8% [12].

Besides interfacial adhesion, filler alignment is also among the main requirements for effective reinforcement in polymer-based system [13]. Attempts to regulate the aligned morphology of CNTs can be categorized into two ways. One is physical blending such as high shear melt mixing, mechanical stretching, fiber and film forming [14-19]. With these methods, the researches of high novelty focused on controlling the degree of CNT orientation in a fine way, the reinforcement is but not ideally achieved. The other way to regulate the morphology of CNTs in polymer matrix is *ex-situ* alignment such as spin-coating or casting polymer solution onto CNT bundles grown by chemical vapor deposition (CVD) method, by which excellent anisotropic electric conductivity is achieved [20-24]. However, poorly wetted by matrix, the densely grown CNTBs would undergo irreversible slipping of the nanotubes within the bundles, resulting in partial failure of filler network. Thus, no mechanical reinforcement in composites with *ex-situ* alignment of CNTs is reported [25-29].

We developed a facile method to regulate the morphology of the nanotubes in OBC matrix. Strong sonication is first used to break the MWCNT bundles (CNTB) into much smaller bundles with better dispersibility, after which mix solvent solution blending method was carried out to prepare OBC/CNTB nanocomposites. The sonication time is short enough to maintain the integrity of nanotubes, and inside the smaller bundles, nanotubes present a well aligned structure. Additionally, a typical HSK structure is observed in OBC matrix with incorporation of CNTBs. In our study, dramatic reinforcement is achieved, i.e., from 7.34 MPa to 24.11 MPa with 2 wt% incorporation of CNTBs.

With direct evidence of bundled morphology of CNTBs in OBC matrix and HSK superstructure, the effect of which on the structural evolution of OBC/CNTB nanocomposites is probed by synchrotron radiation techniques. With *in-situ* small-angle X-ray scattering (SAXS) and wide-angle X-ray diffraction (WAXD) studies of OBC and nanocomposites during deformation, we observed an unexpected inverse evolution trend of long period in nanocomposites compared to that in neat matrix. Additionally, the Herman's orientation factor of both crystal and amorphous phases of nanocomposites is remarkably lower than that of neat sample in the strain range of 0 to 1000%. The HSK superstructure in this low-crystallinity matrix is of high importance in this research, it enables us to give a comprehensive explanation of the structural evolution of OBC nanocomposites during uniaxial deformation.

2. Experimental

2.1 Materials

The INFUSE® OBC used in this study are purchased from local supplier with M_w=82600, M_w/M_n=2.3, soft block segment of 75%, total octene content of 12.9% and overall density of 0.878g/cm^3. CNTB of outer diameter 10-20 nm, length 10-30 μm and specific area >180 m$^2\cdot$g^{-1} were purchased from Chengdu Organic Chemicals Co. Ltd., Chinese Academy of Science. SEM image of CNTBs are shown in Figure 1. Xylene (AR grade) and N,N-dimethyl formamide (DMF) (AR grade) were purchased from Chengdu Kelong Chemical Reagent Factory (China).

2.2 Preparation of OBC Nanocomposites

OBC pellets were dissolved in xylene at 130 ℃ by magnetic stirring in an oil bath. CNTB were dispersed in DMF at the concentration of 1 mg/mL and sonicated with a Sonics Vibra Cell VC-1500 (Sonics & Materials Inc.) at 1200W for 20 min. The DMF/MWCNTs suspension was added dropwise into the xylene/OBC solution after sonication and the mixture was continuously stirred for another 10 min. The mixture was transferred to a rotary evaporator and dried in a vacuum oven at 70 ℃ for 24h to remove residual solvent. Nanocomposite samples were molded at 190 ℃ into films of about 1 mm. Nanocomposites with two CNTB content were prepared, i.e., 2% and 10%, and are designated as CNTB2 and CNTB10, respectively. Before transmission electron microscope (TEM) measurements, CNTB2 was extracted by boiling xylene in Soxhlet extractor for 48 h to remove OBC matrix, the residual MWCNTs were collected and used for characterization.

2. 3 Characterization

Transmission electron microscope (TEM, FEI Tecnai G2 F20 S-TWIN) measurements at an accelerating voltage of 200 kV were carried out to investigate the dispersion state of CNTBs in OBC matrix and the surface morphology of extracted CNTBs. Ultra-thin sections were prepared using a Leica Ultracut UCT ultramicrotome with a diamond knife at -100 ℃, which is well below the glass transition temperature of OBC soft segments.

DSC tests were performed on a Q200 (TA Instruments). Annealed specimens weight about 7-8 mg were heated to 190 ℃ at 5 ℃/min, holding for 5 min to eliminate any thermal history and cooled at 5 ℃/min to 40 ℃. The heat flow was recorded.

Tensile tests were carried out on an Instron 5567 universal testing machine with a 1000N-load cell at room temperature. All specimens of different CNTB concentrations were tested with a gauge length of 20 mm and strain rate of 100 mm/min. 5 samples were tested for each concentration.

Dynamic mechanical measurements were conducted on a DMA Q800 instrument (TA Instruments) in tension film mode with the sample dimension of about 30 mm (length) × 7 mm (width) × 1 mm (thickness). The glass transition temperature of OBC β relaxation is about -45 ℃, we carry out multi-frequency tests in temperature scanning mode in the range of -80 to 0 ℃ to cover the whole temperature range of β relaxation. The ramping rate was 2 ℃/min, and six frequencies were selected from 0.6 to 20 Hz. Temperature control was achieved via liquid nitrogen gas flow.

In situ SAXS and WAXD studies were carried out at the BL16B beamline in the Shanghai Synchrotron Radiation Facility (SSRF). The wavelength used was 0.1237 nm. 2D WAXD and SAXS patterns were collected by a MAR CCD X-ray detector (MAR-USA) with an acquisition time of 20 s for each data frame. The sample-to-detector distance was 2835 mm for SAXS, and was 166 mm for WAXD. All X-ray images were corrected for background scattering, air scattering, and beam fluctuations. Uniaxial tensile deformation was performed with a home-made drawing machine. The samples were stretched symmetrically along the vertical direction with an initial gauge length of 20 mm and strain rate of 20 mm/min. The SAXS and WAXD tests for each sample were carried out separately.

3. Results and discussion

3. 1 Morphology and crystallization behavior of OBC/CNTB nanocomposites

TEM image of CNTB2 are shown in Figure 2a-2h. From Figure 2a and 2b, we can find that after strong sonication and solution blending, the CNTBs are broken down into smaller bundles,

which consist of small scope nanotube aggregate structure at the scale of hundred nanometers and are fully wetted by OBC matrix. This dispersion state of CNTBs in OBC matrix has essential distinction from large scale agglomeration of nanotubes in polymer matrix. From the partial enlarged Figure 2c-2h, we can find that inside the small CNTBs, carbon nanotubes showed a well aligned structure.

A typical morphology of the Soxhlet extracted CNTBs are shown in Figure 3. From Figure 3, it is obvious that the extracted CNTBs remain a bundle structure, and the nanotube inside the bundle form central stem (shish) while OBC crystals are induced to grow approximately perpendicular to the nanotube axis. Thus we can classify the hybrid crystal structure as the hybrid shish-kebab (HSK) superstructure. The periodicity of the HSK superstructure in Figure 3 is not as regular as those in high-crystallinity matrix such as HDPE and PA6,6 [1], which is due to the relatively short hard block length and low hard block content in OBC chain.

The DSC melting and subsequent crystallization curves of OBC/CNTB nanocomposites are presented in Figure 4. The values including onset crystallization temperature T_c, crystallization peak temperature $T_{c,peak}$, melting temperature T_m and crystallinity X_c are listed in Table 1. A strong heterogeneous nucleating effect can be noticed with an increased T_c of 121.7 ℃, compared to 112.1 ℃ of neat OBC, indicating that crystallization begins from the surface of CNTBs. The T_m of OBC nanocomposites are also found to be slightly increased, compared to neat OBC, which could be due to higher $T_{c,peak}$ as well as interfacial crystallization that could make crystal lamellaes more thermally stable. For CNTB10, both T_m and X_c decrease due to the confined space brought by overabundant CNTBs that can eliminate crystal maturation.

3.2 Mechanical behavior

Affected by both the crystalline phase and amorphous phase, semi-crystalline polymers exhibits a complex behavior upon stretching [30-33]. Different from those of high crystallinity polymers with a rigid network and formed by extensively grown lamellar and strong interlamellar coupling [34-36], the deformation-induced structural changes of OBC can be described by the slip-link theory [37,38]. Crystal lamellaes are referred as slip-links, which undergo detachment and subsequent reattachment at crystal edges in small-strain region (λ<200%), providing sliding topological constraint and leading to a repartitioning of the network chains till a yield-like plateau is reached. When the strain goes beyond 200% upon stretching, elongated amorphous entanglements come into play and dominate the stress response; meanwhile, fragmented lamellaes became isolated and transform into a fibrillar morphology.

The typical stress-strain curves of NeatOBC and CNTB2 is shown in Figure 4. With incorporation of CNTBs, the mechanical properties is significantly enhanced. Compared to that of NeatOBC, the tensile strength of CNTB2 is tripled, i.e., from 7.34 MPa to 24.11 MPa. While the Young's Modulus increase from 6.87 MPa to 19.01 MPa with incorporation of 2 wt% CNTBs.

The reason of mechanical enhancement could be mainly attributed to two aspects. One is the interfacial crystallization of OBC crystals on the surface of nanotube surface and the interfacial load transfer generated from it. Massive research has proved that load-transfer can be enhanced by constructing interfacial crystallization in filled polymer systems, thus leading to remarkable reinforcement [3,7,39-41]. Additionally, the dimensional stability of HSK superstructure in CNTB2 makes the nanocomposites robust enough to bear a tripled ultimate strength.

The other reason for reinforcement could be the unique morphology of CNTBs in OBC matrix as well as the low compliance of the rigid HSK superstructure combined by OBC crystals and CNTBs. For reported CNTBs incorporated polymer systems, low inter-tube distance of CNTBs makes itself difficult to be sufficiently wetted by polymer matrix [42]. From TEM figures in Section 3.1, we can find that the nanotubes inside CNTBs are fully wetted by OBC matrix, thus the inter-tube friction in the bundles is maximized. With maximized inter-tube friction and large volume, the rigid HSK structure would stay static under a much higher stress is applied, thus exhibiting a much higher yield-like plateau as well as remarkably improved Young's modulus. The structural changes of OBC nanocomposites during deformation needs to be further investigated.

3.3 Lamellar structural evolution of OBC and nanocomposites during stretching by SAXS analysis

Representative 2D SAXS and WAXD patterns of NeatOBC and CNTB2 during uniaxial deformation at room temperature are shown in Figure 6. The 2D SAXS patterns of unstretched samples both exhibit a broad scattering peak, and no meridional maxima is observed, indicating the inexistence of lamellar stack morphology in OBC matrix [43]. In OBC and its nanocomposites, scattering intensity profiles are both found to decrease monotonically, and the total intensity of CNTB2 sample was much higher than that of NeatOBC. The increase in intensity could be attributed to the void scattering of CNTBs with tube structure [44]. The Lorentz-corrected curve of NeatOBC exhibit a q_{max} value of 0.2396 nm^{-1}, while that of CNTB2 exhibits two maxima, one at 0.1719 nm^{-1} and the other at around 0.8066 nm^{-1}. The second maxima of CNTB2 can be due to the scattering from kebabs of HSK superstructure or the scattering from CNTB phase. For a further confirmation of the second maxima, we carried out a heating process for CNTB2, and SAXS results are provided in Supporting Information S1, from which we can find that the q_{max} of the maxima shifts slightly to higher q values during the melting process, and the maxima still exists even after the matrix is completely melted. We conclude that the second maxima is due to the scattering from the CNTB phase, and the slight shift of q_{max} could be due to the melting of polymer layers wrapping around the nanotube surface which act as the thin shell of nanotube shish.

The long period, $L=2\pi/q_{max}$, can be calculated from Lorentz-corrected integrated 1D curves from the inset of Figure 7. It was determined that with 2 wt% incorporation of CNTBs, L increase from 26.21 nm to 36.53 nm. Researches have reported the increase of long period of nanocomposites with addition of nano-fillers, and two reasons are given: one could be lamellar thickening for the growth of large crystals promoted by nano-fillers such as CNTs, the other possible reason could be the scattering from the filler phase [45-47]. The long period of OBC can be concluded as the size of grain-like local domains, which is the sum of lamellar thickness and amorphous phase between two lamellaes. While for HSK crystal structure, the long period is the distance between two kebabs, which is also marked in the TEM image in Figure 3. The distance between two kebabs in the HSK superstructure in CNTB2 is observed to be around 50 nm. Thanks to low crystallinity of OBC in this study, a considerable proportion of hard segments of OBC

chain can aggregate on the surface of CNTBs and form kebabs, and the density of scattered lamellaes in CNTB2 is smaller than that in NeatOBC. Thus the size of amorphous phase between two dispersed lamellaes in CNTB2 is increased, leading to increase in long period. The long period contributed by HSK superstructure and scattered lamellaes in CNTB2 are both larger than that in NeatOBC, thus the long period of CNTB2 is remarkably higher.

As is presented in Figure 6, the broad scattering peak of both samples evolved into equatorial streak and became sharper with increasing strain upon stretching. For NeatOBC, the equatorial streaks is sharper than those of CNTB2 at same strain. Lorentz-corrected SAXS intensity profiles along the meridian in NeatOBC and CNTB2 at differet strains are shown in Figure 8. The q_{max} of NeatOBC shifts to higher q value with increasing strain, indicating that lamellaes in OBC matrix are broken into smaller but larger density of lamellaes in OBC matrix at higher strains [48]. Unexpectedly, the q_{max} of CNTB2 shifts to lower q value with increasing strain, and the curves show no q_{max} within the experimental limit of SAXS when the strains are beyond 600%, this could be due to that the q_{max} is covered by the large scattering intensity at low q values or the q_{max} of CNTB is beyond the detection range of SAXS. While the q_{max} from the scattering of CNTB phase showed no notable shift. The calculated meridional long periods of NeatOBC and CNTB2 are listed in Figure 9. For NeatOBC, the long period decrease monotonically, which is consistent with previous observation on OBCs [48]. The change of long period of NeatOBC during stretching is dominated by the density of crystal lamellaes. The fragmentation of crystal lamellaes in NeatOBC leads to a higher density of smaller lamellaes, thus the long period between adjacent lamellae layers decreases. While for CNTB2, the long period increase sharply in the strain range of 0-400%. The increase of long period of neat polymer during stretching has been reported in PE, Fluorinated Ethylene-Propylene (FEP) copolymer and poly(urethane-urea), the reasons of which is the increased separation of crystal lamellaes in the stacks [43,49,50]. With a considerable proportion of crystals attached on the surface of CNTBs to form HSK superstructure, the dispersed crystal lamellaes in CNTB are of lower density than that in NeatOBC. In this case, the change of long period of CNTB2 is dominated by the deformation process. Upon uniaxial deformation, the fragmented lamellaes were stretched along the stretching direction, thus the long period increases, which conforms to the evolution mechanism of long periods in FEP copolymer and poly(urethane-urea). The illustration of the structural evolution and change in long period of both NeatOBC and CNTB2 are presented in Figure 10.

3.4 Structural analysis by WAXD during deformation

Before deformation, the WAXD patterns of NeatOBC and CNTB2 both exhibit isotropic rings of amorphous reflection as well as orthorhombic (110) and (200) reflections. As is reported, the (110) reflection of OBC becomes four-arc-like with maximum at the off-axis position at the strain of 200%, which indicates a tilted structure formed with respect to the stretching direction, and the four arcs change to two arcs at the strain of 500% [48]. S.L. Aggarwal has given the explanation that the splitting of the (110) reflection is due to imperfect orientation of b- and c-axis with respect to the stretching direction, i.e., there are considerable wobble of the *b*- and *c*-axis [51]. The four-arc pattern is not very obvious in our results, but the splitting of (110) reflection and subsequent approaching can also be observed, which is presented and discussed in detail later. At the onset strain of 600%, (010) reflection of the strain-induced monoclinic crystals emerges on the equator between amorphous ring and (110) reflection in WAXD patterns, exhibiting a highly ordered but relatively diffuse point-like reflection.

Selected 1D WAXD profiles of NeatOBC and CNTB2 during deformation at different strains are listed in Supporting Information S2. The total fraction of orthorhombic form of OBC and nanocomposites can be calculated by estimating the total area of (110) and (200) reflection [48], which is listed in Figure 11. In slip-link dominated region (λ<200%), the slope of fraction decrease for NeatOBC is sharper than that of CNTB2, which could be due to the heterogeneous stress distribution brought by HSK superstructure in CNTB2. With load transferred to robust HSK superstructure, the load on dispersed lamellaes were lower in CNTB2, thus the repartitioning of the network is more gentle, and the fraction decrease of orthorhombic crystals is more inconspicuous. With increasing strains, the difference of orthorhombic fraction between NeatOBC and CNTB2 gets larger. For NeatOBC, the mechanical melting and transformation of orthorhombic crystals into monoclinic crystals brings decrease to the fraction of orthorhombic crystals. While in CNTB2, the HSK structure is of higher dimensional stability, and transformation of kebabs into monoclinic crystals would be more difficult to take place.

The orientation degree of orthorhombic crystal and amorphous crystal phases can be calculated by the Hermans' orientation function [52]:

$$f = \frac{3\langle \cos^2 \varphi\rangle - 1}{2} \quad (1)$$

where φ is the angle between the chain axis and the reference axis (stretching direction). $\langle \cos^2 \varphi \rangle$ is defined as

$$\langle \cos^2 \varphi \rangle = \frac{\int_0^{\pi/2} I(\varphi)\ \cos^2 \varphi \sin \varphi \mathrm{d}\varphi}{\int_0^{\pi/2} I(\varphi) \sin \varphi \mathrm{d}\varphi} \quad (2)$$

where *I(φ)* is the scattered intensity along the angle φ. The value of f is in the range of -0.5 to 1. f = 1 indicates perfect alignment of all polymer chains along stretching direction; when f = -0.5, it means that the chains are all aligned perpendicularly to the stretching direction; f = 0 indicates random orientation of the chains. The crystal orientation in this case can be indirectly obtained from the (110) and (200) reflections with the following expression [48].

$$\langle \cos^2 \varphi \rangle = 1 - 1.435\langle \cos^2 \varphi_{110} \rangle - 0.565\langle \cos^2 \varphi_{200} \rangle \quad (3)$$

The calculated *f* value of amorphous phase was actually that of the normal vector of the amorphous chains. Thus, the *f* value need to be multiplied by a factor of -2 in order to convert the orientation factor (-0.5 to 0) into the value (1 to 0), which represent the degree of orientation along the deformation axis. As for both orthorhombic crystal and amorphous phases, the contribution from the (010) reflection in the azimuthal intensity distribution can be perfectly subtracted with Gaussian peak fitting, which is shown in Supporting Information Figure S3.

The calculated *f* values for orthorhombic and amorphous phases as a function of strain is shown in Figure 12. The *f* value of orthorhombic crystals of both NeatOBC and CNTB2 increase sharply at the strain range of 0-600%, and the *f* values of orthorhombic crystals of CNTB2 is relatively smaller than that of NeatOBC in this strain range. On whether nanofillers can promote the structural evolution of crystalline polymers or hinder it, different mechanisms has been proposed. B.S. Hsiao et al. reported that the incorporation of 1D fillers such as carbon nanofibers (CNFs) and fluorinated MWCNTs can bring heterogeneous stress distribution in polyolefin matrix, leading to reduced stress on crystals, thus the degree of orientation is

lower; physical constraint effect of fillers can also reduce the degree of crystal orientation [43,44]. While as is reported by N.S. Murthy et al., CNTs in solution- and gel-spun polyacrylonitrile (PAN) fibers can facilitate the orientation of PAN crystals during deformation [53]. Y.F. Men and coworkers reported similar results that the 2D montmorillonites (MMTs) can incorporate into the synergistic movement of PE and MMTs, resulting in increased degree of orientation [54]. Our observation seems to be consistent with that of B.S. Hsiao's. The load-transfer brought by HSK structure could surely release a certain amount of stress from the matrix. Additionally, we carried out dynamic mechanical multi-frequency tests in temperature scanning mode in the range of -80 to 0 ℃ to investigate the physical constraint effect of CNTBs on the amorphous β-relaxation of OBC chains (DMA curves and the calculation of activation energy of glass transition of NeatOBC and CNTB2 is listed in Supporting Information Figure S4). The calculated activation energy E_a of glass transition of amorphous phase is 236.11 kJ for NeatOBC and 236.50 kJ for CNTB2, indicating that the incorporation of CNTBs has no obvious effect on the chain mobility of surrounding soft segments. Since the presence of HSK structure does not affect the soft segment mobility, we decide to use chain connectivity and network efficiency to interpret the difference in f values between NeatOBC and CNTB2. As is reported, for olefin random copolymer (ORC), a statistical block length distribution leads to more but shorter hard blocks and soft segments in one polymer chain, thus a single polymer chain in ORC can participate in more fringed crystal junctions; while for OBC with both long hard and amorphous segments, chains can only be involved in fewer lamellar crystal junctions, indicating a lower chain connectivity and network efficiency than that of ORC, thus the orientation factor of both crystal and amorphous phases of OBC are lower than those of ORC [47]. Even for OBCs with different block architectures, if the polymer chains are involved in fewer folded-chain lamellar crystals, the orientation factor of both crystal and amorphous phases would be lower [55]. With incorporation of CNTBs, the large surface area of nanotube bundles structure can act as template for interfacial crystallization, thus after crystallization-induced phase segregation, HSK structure in CNTB2 act like much larger but fewer hybrid crystal junctions. In this case, the OBC chains in CNTB2 are involved in even fewer physical junctions, indicating that the connectivity and network efficiency of CNTB2 is lower than that of NeatOBC. Thus the f value of both orthorhombic crystal and amorphous phases of CNTB2 are lower than those of NeatOBC. Additionally, the low compliance of HSK superstructure could also contributed to decreased f values of orthorhombic crystal phase. When the strain exceeds 1000%, the increase of f value of orthorhombic crystal phase of both samples slows down, indicating a sufficient orientation of orthorhombic crystals. In this region, the f values of orthorhombic crystal phase of NeatOBC and CNTB2 become close, and the f value of CNTB2 is even slightly higher when the strain goes beyond 1200%. This could be due to that the difference of network efficiency is smaller when the dispersed lamellaes in both samples became sufficiently fragmented. At these strains, the structure evolution is mainly about the extension of the amorphous segments along the stretching direction

As is widely reported, the incorporation of nanofillers can retard the tilting of lamellar stacks [43,44]. Figure 15 shows the changes of the angle (ψ) between the lamellaes and the stretching direction. In our observation, the tilting of lamellaes exists during the whole deformation process when the strain reaches 200%. It can be noted that ψ of both samples decrease quickly at low strains (<600%), above which the decrease slowed down till the samples broke (The selected azimuthal intensity distribution curves of the (110) reflection of NeatOBC are presented in Supporting Information Figure S5). Additionally, the ψ values of CNTB2 is lower than that of NeatOBC, and the difference becomes smaller upon stretching

3.5 Orientation of CNTBs in OBC matrix

To probe the orientation of CNTBs in OBC matrix, CNTB10 with 10 wt% of CNTBs is prepared for WAXD analysis. The stress-strain curve as well as selected WAXD patterns are presented in Figure 14. The elongation at break of CNTB10 is much smaller than that of NeatOBC due to the physical constraint brought by high incorporation of CNTBs. From Figure 14 we can see that unstretched CNTB10 exhibit a uniform ring of (002) reflection of CNTBs. Upon stretching, a preferred orientation of CNTBs along the stretching axis occurs, exhibiting concentrated intensity of (002) CNTB reflection on the equator. Figure 15 shows the 2D WAXD patterns of CNTB10 at the strain of 1200%, the attached rectangular panel exhibits the 2D intensity with diffraction angle 2θ and azimuth angle plots. From the rectangular panel we can see that the concentrated intensity at the azimuth angle of 90^o and 270^o is not completely symmetric along the diffraction angle axis. This is due to the contribution from the highly oriented by relatively diffused (010) monoclinic reflection, which can also be subtracted with Gaussian peak fitting (the subtraction is presented in Supporting Information Figure S6).

As is shown in Figure 14, the CNTB10 exhibits two-arc (110) reflection at all strains above 200%, indicating that high incorporation of CNTBs can prevent the tilting of crystal lamellaes in OBC matrix, which is consistent with the decreased ψ values of CNTB2 compared to NeatOBC. The Hermans' orientation factor f of orthorhombic crystal, amorphous and CNTBs phases as a function of varying strains are listed in Figure 18. From Figure 16 we can see that the orientation behavior of CNTB10 during stretching is of large difference from that of NeatOBC and CNTB2. For NeatOBC and CNTB2, the evolution of orientation of both crystal and amorphous phases comply with the slip-link theory. The crystals orientation of NeatOBC and CNTB2 is fast at low strains and slows down at intermediate strains till maximum is reached, while f values of amorphous phase are much lower than those of crystal phase. For CNTB10, the f values of crystal phase are much lower than those of NeatOBC and CNTB2, indicating prominent stereo hindrance brought by the dense network of CNTBs. Additionally, the f value of amorphous phase at low-strain region is even slightly higher than that of orthorhombic crystal phase, indicating that the mobility of orthorhombic crystals are more constrained by the rigid network of CNTBs, and deformation of CNTB10 sample at low strains might be more contributed by the extension of soft segments. Thus we can deduce that the slip-link theory doesn't work for the structural evolution of CNTB10. The f value of CNTBs increase upon stretching, but the increase of f value is significantly lower than that of orthorhombic crystals. This could be due to that the rigid network brought by high incorporation of CNTBs is of much lower compliance than that of OBC matrix, which is consistent with previous research [43].

4. Conclusions

OBC/CNTB nanocomposites is prepared by short-time strong sonication of CNTB suspension and subsequent solution blending. Inside the incorporated CNTBs that consist of several to dozens of nanotubes, the nanotubes exhibit a well aligned structure. A typical HSK superstructure is observed in TEM results that the nanotubes in CNTBs act like central shish and OBC crystals perpendicularly decorate the tube surface. The tensile strength and Young's modulus of nanocomposites are both triple with 2 wt% incorporation of CNTBs. The reinforcement might be due to interfacial crystallization as well as the low compliance of network brought by the unique CNTB morphology. With synchrotron SAXS and WAXD techniques, the structural evolution process of OBC and nanocomposites are thoroughly investigated. The HSK structure in CNTB2 attract a considerable proportion of OBC crystals and the dispersed lamellaes are of lower density than that in NeatOBC. The larger long period of HSK superstructure in CNTB2 and increased size of amorphous phase between adjacent lamellaes both contribute to the remarkable increase in long period. The change of long period of NeatOBC upon stretching is dominated by the density of lamellaes. The lamellae density is increased with the fragmentation of lamellaes during stretching, leading to decreased long period. Inversely, the long period of CNTB2 increases during stretching and exceed the SAXS limit above the strain of 400%. With lower density of scattered crystal lamellaes, the change of long period of CNTB2 is dominated by the deformation process, and the increased separation of crystal lamellaes leads to increase in long period. The orientation behaviors of NeatOBC and CNTB2 both comply with the slip-link theory that the orientation of crystal lamellaes develops fast at low strains and slows down at intermediate strains, while the amorphous phase exhibit slow but continuous orientation during the whole deformation process. The difference in Hermans' orientation factor of NeatOBC and CNTB2 upon stretching is explained by the difference in chain connectivity and network efficiency between both samples. The HSK superstructure act as much larger but fewer hybrid crystal junctions, thus the OBC chains in CNTB2 are involved in even fewer physical junctions, indicating that the connectivity and network efficiency of CNTB2 is lower than that of NeatOBC. Thus the Hermans' orientation factor of both crystal and amorphous phases of CNTB2 are lower than that of NeatOBC. The incorporation of CNTBs can also retard lamellar tilting during the deformation process, and at high incorporation of 10 wt% CNTBs, the lamellar tilting is totally absent. The orientation behavior of CNTB10 doesn't accord with the slip-link theory, which is due to the prominent stereo hindrance brought by the rigid CNTB network with high incorporation of CNTBs. The orientation of CNTBs in CNTB10 develops significantly slower than that of orthorhombic crystals, indicating that the rigid network of CNTBs is of much lower compliance than that of matrix.

Acknowledgements

The authors would like to thank the National Basic Research Program (973 program) (No. 2011CB606000) for financial support.

Notes and references

[a]*College of Polymer Science and Engineering, State Key Laboratory of Polymer Materials Engineering, Sichuan University, Chengdu 610065, People's Republic of China*

(1). C.Y. Li, L.Y. Li, W.W. Cai, S.L. Kodjie, K.K. Tenneti. *Advanced Materials* **2005**, 17: 1198-202.
(2). C.Y. Li, L.Y. Li, C.Y. Ni. *Journal of the American Chemical Society* **2006**, 128: 1692-9.
(3). S. Zhang, M.L. Minus, L. Zhu, C.P. Wong, S. Kumar. *Polymer* **2008**, 49: 1356-64.
(4). C. Wang, C.R. Liu. *Polymer* **1999**, 40: 289-98.
(5). N.Y. Ning, S.R. Fu, W. Zhang, F. Chen, K. Wang, H. Deng, Q. Zhang, Q. Fu. *Progress in Polymer Science* **2012**, 37: 1425-55.
(6). J.Z. Xu, G.J. Zhong, B.S. Hsiao, Q. Fu, Z.M. Li. *Progress in Polymer Science* **2014**, 39: 555-93.
(7). J.H. Yang, C.Q. Wang, K. Wang, Q. Zhang, F. Chen, F. R.N. Du, Q. Fu. *Macromolecules* **2009**, 42: 7016-23.
(8). C.Y. Li, L.Y. Li, C.Y. Ni, L.X. Rong, B.S. Hsiao. *Polymer* **2007**, 48: 3452-60.
(9). L.Y. Li, B. Li, G.L. Yang, C.Y. Li. *Langmuir* **2007**, 23: 8522-5.
(10). Z.W. X. Qun, Z.M. Chen, J. Yue. *Macromolecules* **2008**, 41: 2868-73.
(11). N.Y. Ning, W. Zhang, Y.S. Zhao, C.Y. Tang, M.B. Yang, Q. Fu. *Polymer* **2012**, 20: 4553-9.
(12). H.P. Wang, D.U. Khariwala, W. Cheung, S.P. Chum, A. Hiltner, E. Baer. *Macromolecules* **2007**, 40: 2852-62.
(13). J.N. Coleman, U. Khan, W.J. Blau, Y.K. Gun'ko. *Carbon* **2006**, 44: 1624-52.
(14). E.T. Thostenson, T.W. Chou. *Journal of Physics D: Applied Physics* **2002**, 35: L77.
(15). Y.A. Kim, T. Hayashi, M. Endo, Y. Gotoh, N. Wada, J. Seiyama. *Scripta Materialia* **2006**, 54: 31-5.
(16). H.Q. Hou, J.J. Ge, J. Zeng, Q. Li, D.H. Reneker, A. Greiner, S.Z.D. Cheng. *Chemical Materials* **2005**, 16: 967-73.
(17). R. Sen, B. Zhao, D. Perea, M.E. Itkis, H. Hu, J. Love, E. Bekyarova, R.C. Haddon. *Nano Letter* **2004**; 4: 459-64.
(18). J.B. Gao, A.P. Yu, M.E. Itkis, E. Bekyarova, B. Zhao, S. Niyogi, R.C.J. Haddon. *Journal of the American Chemical Society* 2004, 126: 16698-9.
(19). J.J. Ge, H.Q. Hou, Q. Li, M.J. Graham, A. Greiner, D.H. Reneker, F.W. Harris, S.Z.D. Cheng. *Journal of the American Chemical Society* **2004**; 126: 15754-61.
(20). C.A. Martin, J.K.W. Sandler, A.H. Windle, M.K. Schwarz, W. Bauhofer, K. Schulte, M.S.P. Shaffer. *Polymer* **2005**, 46: 877-86.
(21). J.K.W. Sandler, J.E. Kirk, I.A. Kinloch, M.S.P. Shaffer, A.H. Windle. *Polymer* **2003**, 44: 5893-9.
(22). H.S. Peng. *Journal of the American Chemical Society* **2008**, 130: 42-3.
(23). B.J. Hinds, N. Chopra, T. Rantell, R. Andrews, V. Gavalas, L.G. Bachas. *Science* **2004**, 303: 62-5.
(24). H.S. Peng, X.M. Sun. *Chemical Physics Letters* **2009**, 471: 103-5.
(25). E.T. Thostenson, Z.F. Ren, T.W. Chou. *Composites Science and Technology* **2001**, 61: 1899-912.
(26). E. Flahaut, A. Peigney, C. Laurent, C. Marliere, F. Chastel, A. Rousset. *Acta Materialia* **2000**, 48: 3803-12.
(27). A. Peigney, C. Laurent, E. Flahaut, A. Rousset. *Ceramics International* **2000**, 26: 667-83.
(28). A. Peigney, C. Laurent, O. Dumortier, A.J. Rousset. *Journal of the European Ceramic Society* **1998**, 18: 1995-2004.
(29). A. Peigney, C. Laurent, A. Rousset. *Key Engineering Materials* **1997**, 132: 743-6.
(30). A. Cowking, J.J. Rider. *Journal of Material Science* **1969**, 4: 1051-8.
(31). A. Peterlin. *Journal of Material Science* **1971**, 6: 490-508.
(32). T. Pakula, M. Trznadel. *Polymer* **1985**, 26: 1011-8.
(33). M. Trznadel, T. Pakula, M. Kryszewski. *Polymer* **1985**, 26: 1019-24.
(34). Z.Y. Jiang, Y.J. Tang, Y.F. Men, H.F. Enderle, D. Lilge, S.V. Roth, R. Gehrke, J. Rieger. *Macromolecules* **2007**, 40: 7263-9.
(35). M. Al-Hussein, G. Strobl. *Macromolecules* **2002**, 35: 8515-20.
(36). Y.F. Men, J. Rieger, K. Hong. *Journal of Polymer Science: Polymer Physics* **2005**, 43: 87-96.

(37). S. Bensason, E.V. Stepanov, S. Chum, A. Hiltner, E. Baer. *Macromolecules* **1997**, 30: 2436-44.
(38). H.P. Wang, H.P. Chum, A. Hiltner, E.J. Baer. *Journal of Applied Polymer Science* **2009**, 113: 3236-44.
(39). M. Cadek, J. Coleman, V. Barron, K. Hedicke, W. Blau. *Applied Physics Letters* **2002**, 81: 5123-5.
(40). F. Mai, K. Wang, N.J. Yao, H. Deng, F. Chen, Q. Fu. *Journal of Physical Chemistry B* **2010**, 114: 10693-702.
(41). S.J. Zhang, W. Lin, C.P. Wong, D.G. Bucknall, S. Kumar. *ACS Applied Materials & Interfaces* **2010**, 2: 1642-7.
(42). A. Kis, G. Csányi, J.-P. Salvetat, Thien-Nga Lee1, E. Couteau1, A.J. Kulik, W. Benoit, J. Brugger, L. Forró. *Nature Materials* **2004**, 3: 153-7.
(43). X.M. Chen, C. Burger, D.F. Fang, I. Sics, X.F. Wang, W.D. He, R.H. Somani, K. Yoon, B.S. Hsiao, B. Chu. *Macromolecules* **2006**, 39: 5427-37.
(44). X.M. Chen, Y. Yoon, C. Burger, I. Sics, D.F. Fang, B.S. Hsiao, B. Chu. *Macromolecules* **2005**, 38: 3883-93.
(45). P. Liu, K.L. White, H. Sugiyama, J. Xi, T. Higuchi, T. Hoshino, R. Ishige, H. Jinnai, A. Takahara, H.J. Sue. *Macromolecules* **2013**, 46: 463-73.
(46). A.B. Espinoza-Martinez, C.A. Avila-Orta, V.J. Cruz-Delgado, F.J. Medellin-Rodriguez, D. Bueno-Baques, J.M. Mata-Padilla. *Journal of Applied Polymer Science* **2014**, 132: 41765.
(47). C.A. Avila-Orta, F.J. Medellin-Rodriguez, M.V. Davila-Rodriguez, Y.A. Aguirre-Figueroa, K. Yoon, B.S. Hsiao. *Journal of Applied Polymer Science* **2007**, 106: 2640-7.
(48). F. Zuo, C. Burger, X.M. Chen, Y.M. Mao, B.S. Hsiao. *Macromolecules* **2010**, 43: 1922-9.
(49). Y.J. Tang, Z.Y. Jiang, Y.F. Men, L.J. An, H.F. Enderle, D. Lilge, S.V. Roth, R. Gehrke, J. Rieger. *Polymer* **2007**, 48: 5125-32.
(50). F.J. Yeh, B.S. Hsiao. *Macromolecules* **2003**, 36: 1940-54.
(51). S.L. Aggarwal, G.P. Tilley, O.J. Sweeting. Journal of Polymer Science **1961**, 51: 551-68.
(52). W.Z. Wilchinsky. *Journal of Applied Physics* **1960**, 31: 1969-72.
(53). W.J. Wang, N.S. Murthy, H.G. Chae, S. Kumar. *Polymer* **2008**, 49: 2133-45.
(54). C.Y. Ren, Z.Y. Jiang, X.H. Du, Y.F. Men, T. Tang. *Journal of Physical Chemistry B* **2009**, 113: 14118-27.
(55). F. Zuo, Y.M. Mao, X.W. Li, C. Burger, B.S. Hsiao. *Macromolecules* **2011** 44: 3670-3.

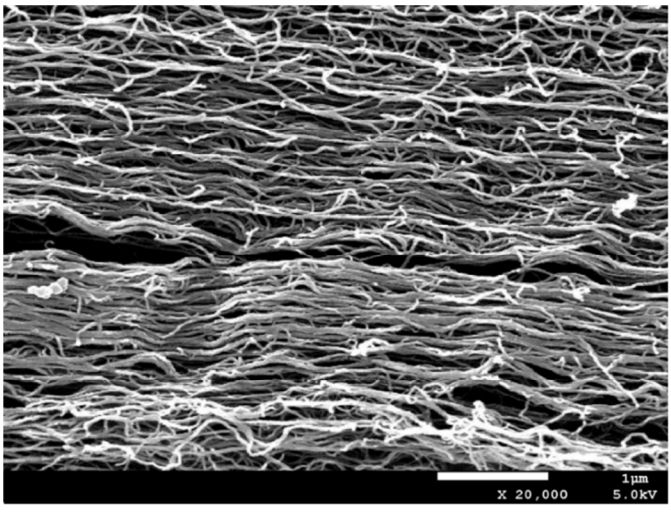

Figure 1. SEM image of raw CNTBs

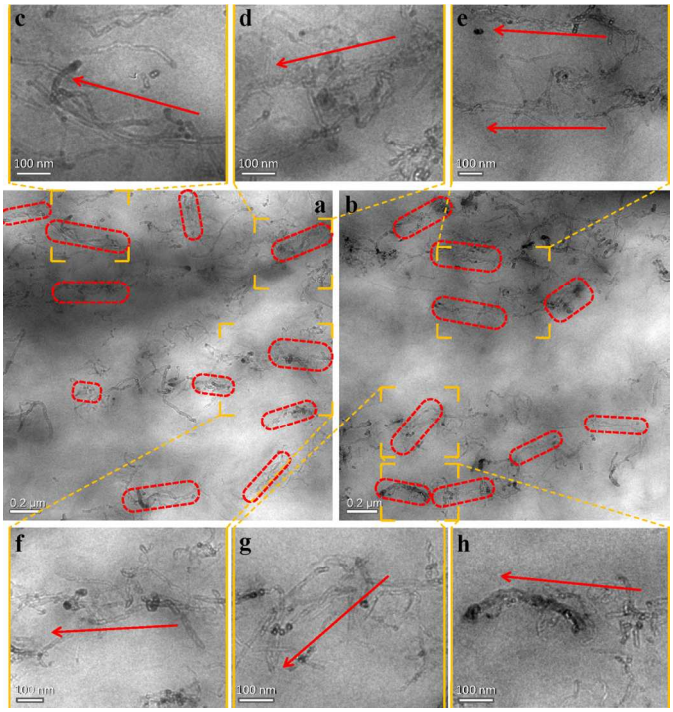

Figure 2. (a, b) TEM image of CNTB2 (Figure 2a and Figure 2b are of different view of the sample, Figure 2c, 2d, 2e, 2f, 2g and 2h are partial enlarged details of Figure 2a and 2b)

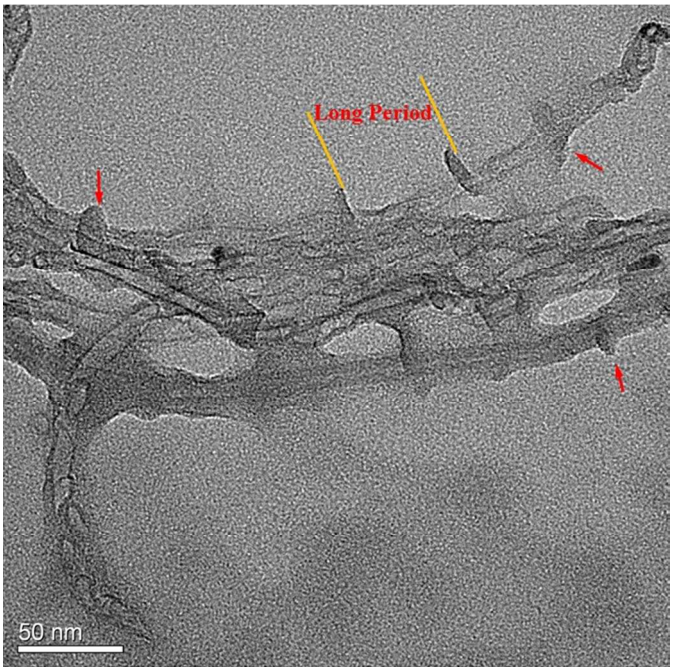

Figure 3. A typical morphology of Soxhlet extracted CNTBs from nanocomposites.

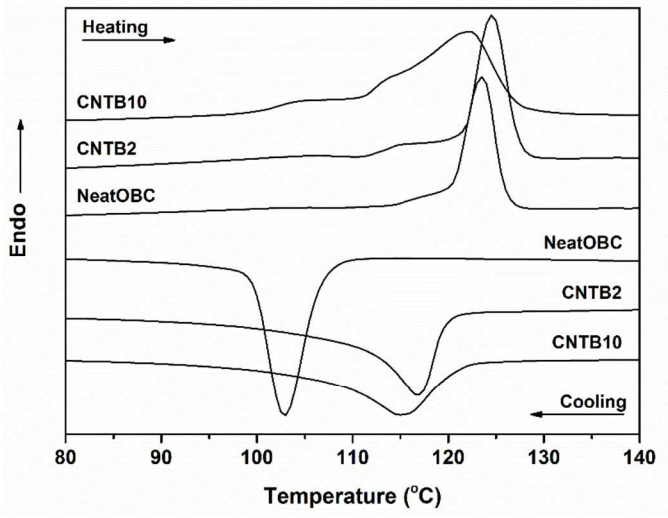

Figure 4. Nonisothermal melting and crystallization curves OBC and nanocomposites.

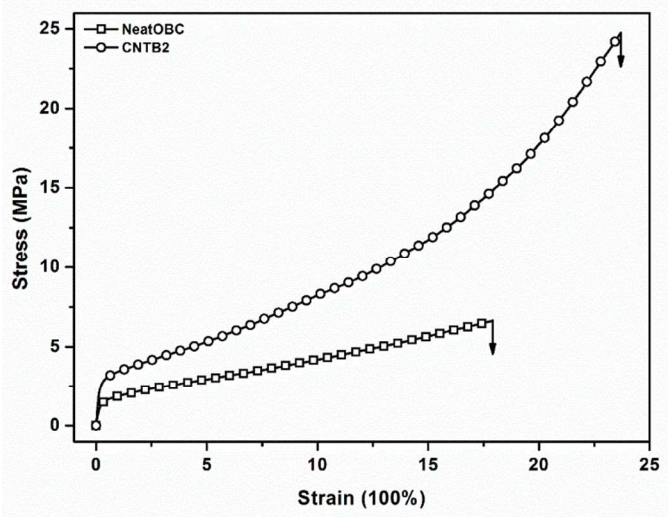

Figure 5. Stress-strain curves for NeatOBC and CNTB2.

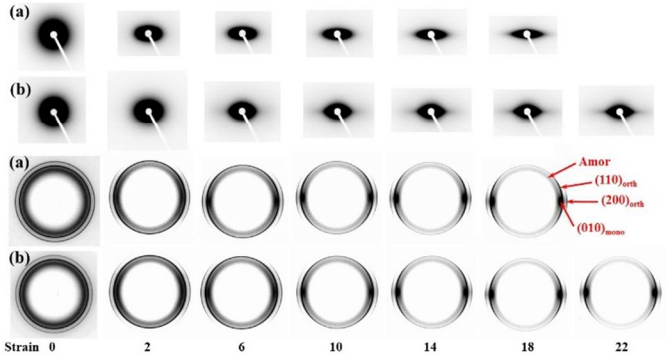

Figure 6. Selected 2D WAXD and SAXS patterns of (a) NeatOBC and (b) CNTB2.

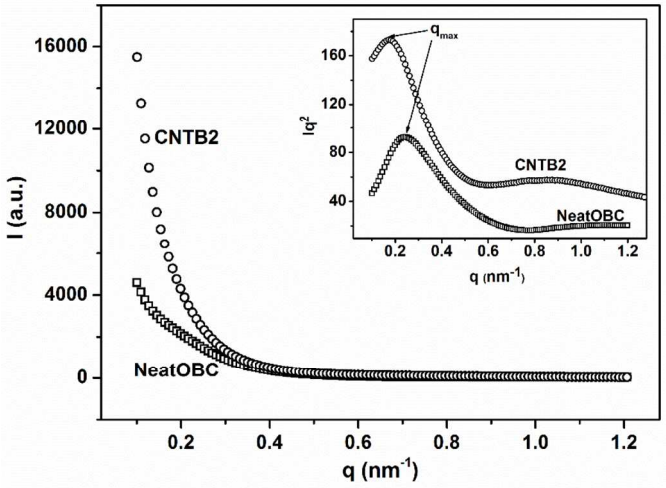

Figure 7. Integrated SAXS profiles of unstretched NeatOBC and CNTB2. The inset picture is the Lorentz-corrected SAXS profiles of NeatOBC and CNTB2.

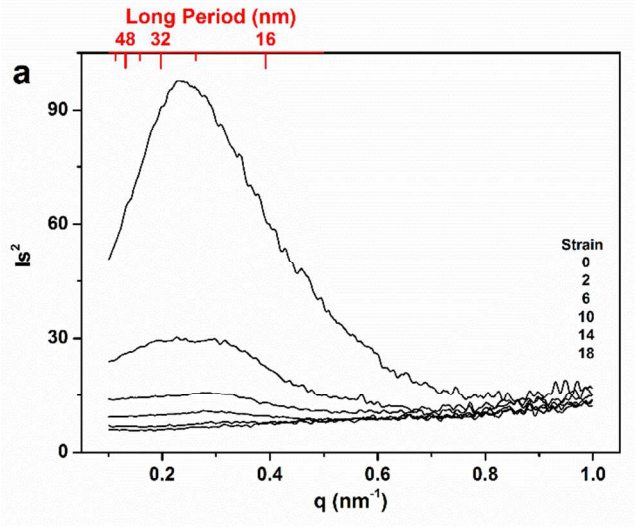

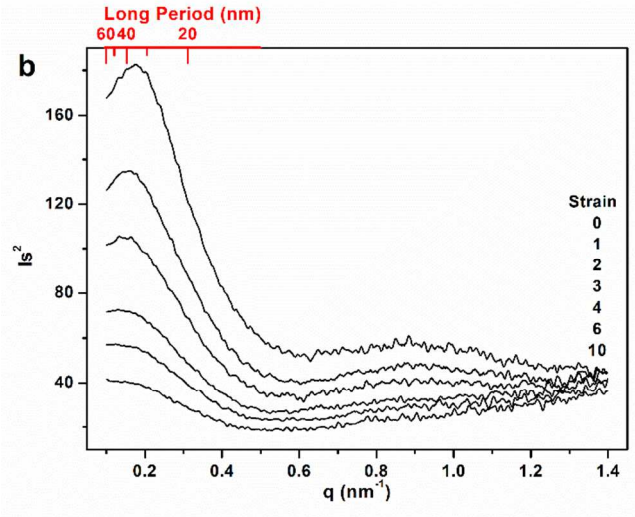

Figure 8. Selected Lorentz-corrected integrated SAXS profiles along meridian of (a) OBC and (b) CNTB2.

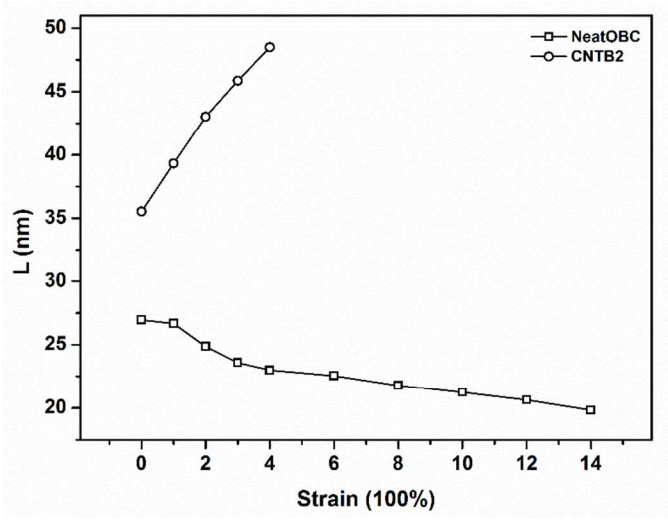

Figure 9. Change of meridional long period of NeatOBC and CNTB2 during deformation.

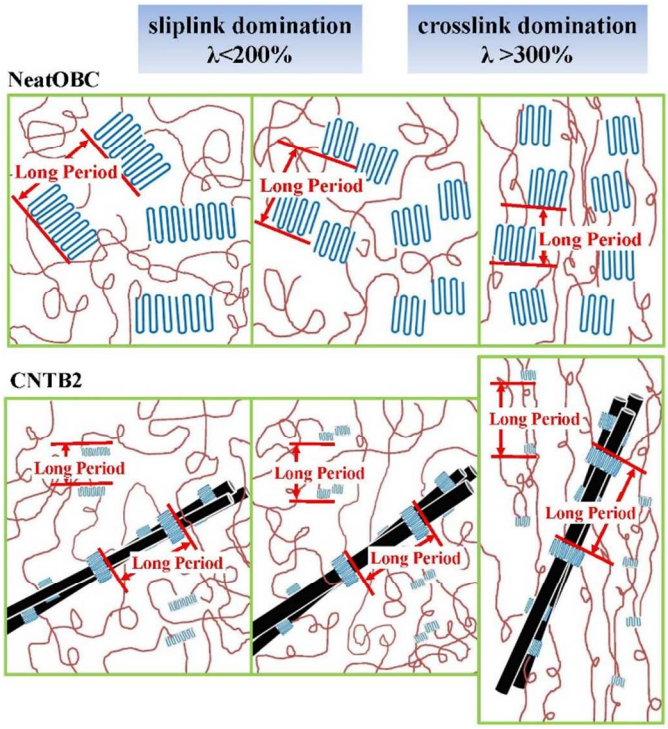

Figure 10. Schematic diagrams of the structural evolution of NeatOBC and CNTB2 during deformation.

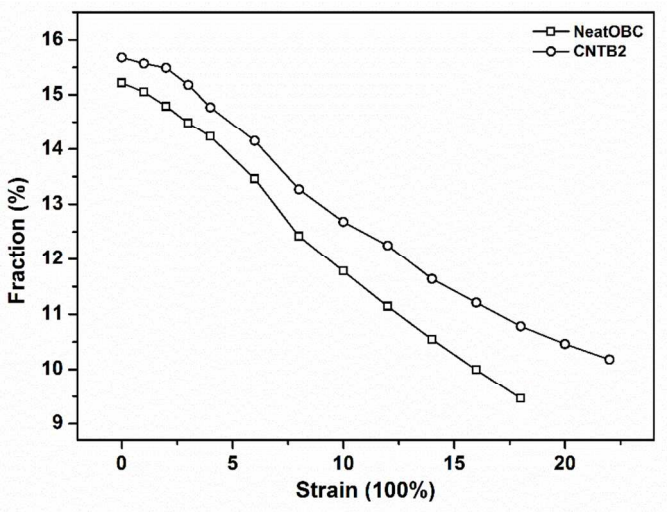

Figure 11. Fraction of orthorhombic crystal in NeatOBC and CNTB2 as a function of strain.

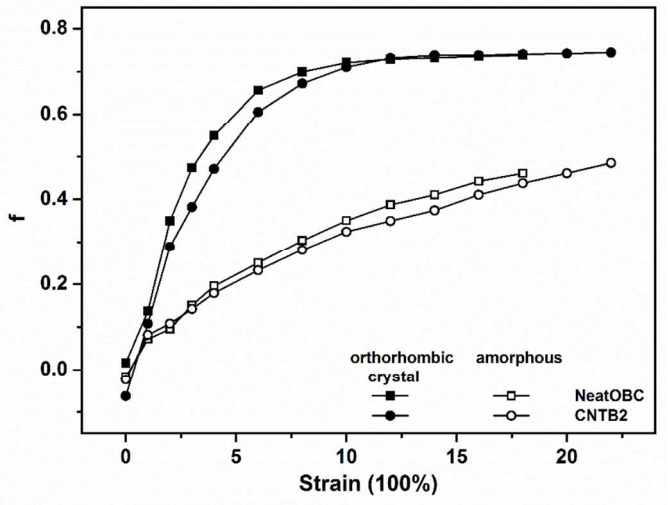

Figure 12. Hermans' orientation factors of orthorhombic crystal and amorphous phases of NeatOBC and CNTB2 as a function of strain.

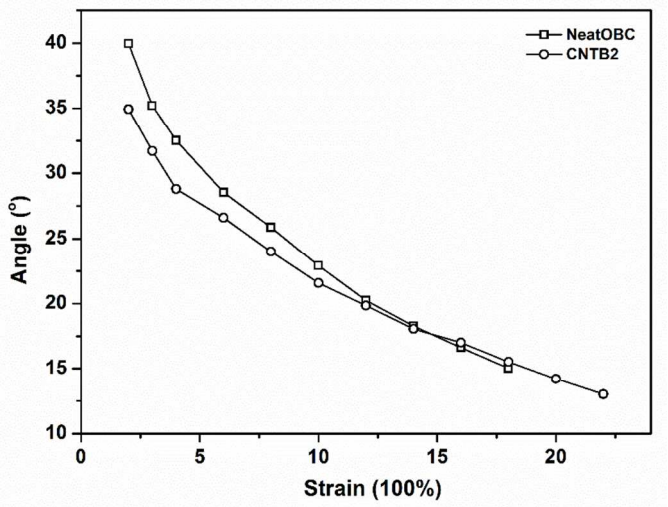

Figure 13. Changes of the angle between the lamellar stack and the stretching direction as a function of strain for NeatOBC and CNTB2.

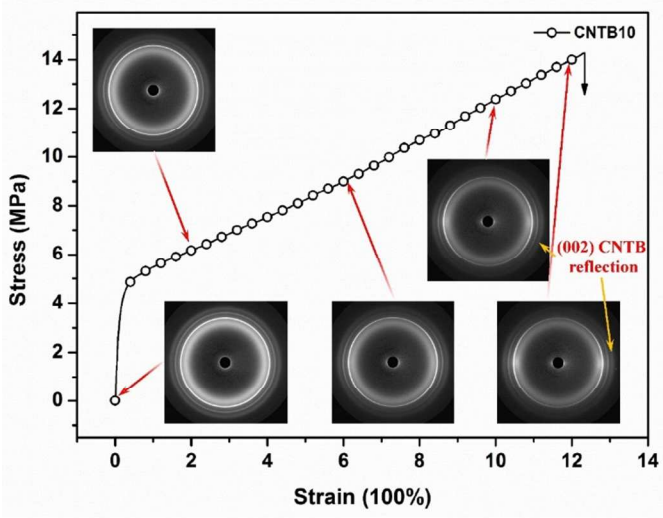

Figure 14. Stress-strain curves and selected WAXD patterns of CNTB10 during deformation.

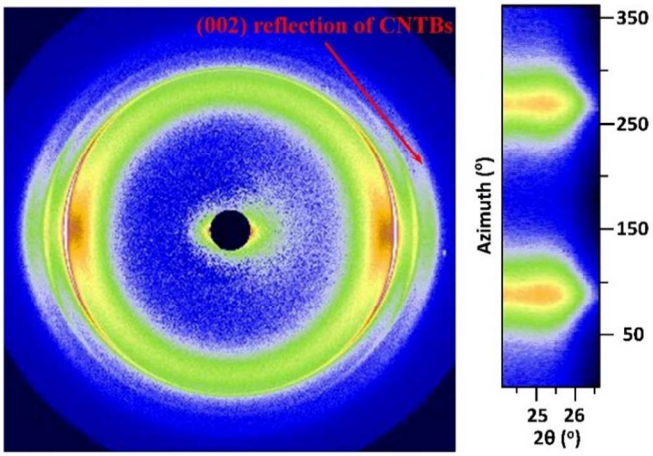

Figure 15. WAXD pattern of CNTB10 at the strain of 1200%. The rectangular panels attached to the WAXD pattern shows the intensity of the (002) reflection of CNTBs with 2θ and azimuth plots.

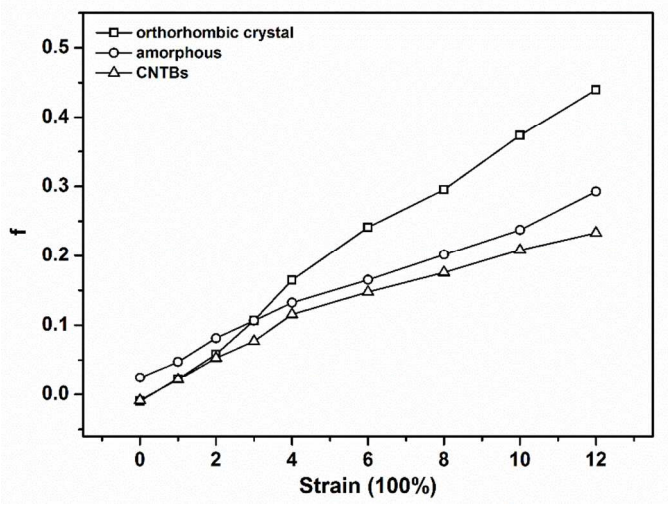

Figure 16. Hermans' orientation factors of orthorhombic crystal, amorphous and CNTB phases of CNTB10 as a function of strain.

Table 1. Data of Nonisothermal crystallization behaviors of OBC and nanocomposites..

Sample Notation	T_c (℃)	$T_{c,peak}$ (℃)	T_m (℃)	X_c (%)
NEAT	112.1	103.9	123.4	14.34
CNTB2	121.7	116.8	123.9	14.76
CNTB10	123.5	115.2	121.2	12.47

Table 2. Data of mechanical properties of OBC and nanocomposites. (+)means positive error and (-) means negative error.

Sample Notation	Tensile Strength (MPa)	Error Bar (MPa)	Young's Modulus (MPa)	Error Bar (MPa)	Elongation at break (100%)	Error Bar (100%)
NEAT	7.34	0.81(+), 0.13(-)	6.87	0.48(+), 0.65(-)	18.01	0.73(+), 0.27(-)
CNTB2	24.11	0.60(+), 0.21(-)	19.01	0.31(+), 0.39(-)	22.95	0.72(+), 0.36(-)
CNTB10	14.30	0.90(+), 0.69(-)	32.15	2.31(+), 3.07(-)	12.32	0.34(+), 0.57(-)